Purdue University
Purdue e-Pubs

Birck and NCN Publications | Birck Nanotechnology Center

2012

End-to-End Modeling for Variability and Reliability Analysis of Thin Film PV

Sourabh Dongaonkar
Purdue University - Main Campus, sourabh@purdue.edu

Muhammad A. Alam
Purdue University - Main Campus

Follow this and additional works at: http://docs.lib.purdue.edu/nanopub


Part of the Electronic Devices and Semiconductor Manufacturing Commons, and the Power and Energy Commons

Dongaonkar, Sourabh and Alam, Muhammad A., "End-to-End Modeling for Variability and Reliability Analysis of Thin Film PV" (2012). *Birck and NCN Publications.* Paper 857.
http://dx.doi.org/10.1109/IRPS.2012.6241828

This document has been made available through Purdue e-Pubs, a service of the Purdue University Libraries. Please contact epubs@purdue.edu for additional information.

End to End Modeling for Variability and Reliability Analysis of Thin Film Photovoltaics

Sourabh Dongaonkar and Muhammad A. Alam
School of Electrical and Computer Engineering
Purdue University
West Lafayette, IN, USA phone: (+1)-(765) 494-5988, alam@purdue.edu

***Abstract*—We present an end-to-end modeling framework, spanning the device, module and also system levels, for analyzing thin film photovoltaics (PV). This approach is based on embedding a detailed, statistically relevant, physics based equivalent circuit into module and array level simulations. This approach enables us to analyze key variability and reliability issues in thin film PV, and allows us to interpret their effect on process yield and intrinsic module lifetimes. Our results suggest that the time-zero gap between cell and module efficiencies, a key variability concern for thin-film PV, can be attributed to process-related shunts with log-normal PDF distributed randomly across the cell surface. Similarly, this end-to-end simulation approach allows us to investigate the reliability issues caused by partial shadowing in thin film modules, especially in context of array configurations. These results provide important insights into its nature and consequences of shadow degradation on long term system performance. This work showcases the importance of an integrated analysis in case of thin film PV, because traditional approaches used to Silicon PV to tackle reliability/variability issues cannot be applied directly to such systems.**

***Index Terms*—thin film PV, variability, reliability, shunt, partial shadow, modeling and simulation**

I. Introduction

Thin film photovoltaics (TFPV) offer attractive alternative to conventional Silicon based PV, due to their low energy and capital costs [1], as well as low-weight and form factors for building integrated applications. Despite these advantages, and even with continually improving cell efficiencies, commercial adoption of thin film PV has been restricted. Besides the rapidly declining cost of c-Si PV, significant challenges in improving the yield and lifetimes of TFPV technologies have been key factors responsible for this problem. One such factor affecting their successful commercialization is a persistent gap between cell (η_C) and module (η_M) efficiency (Fig. 1) [2]. This gap can be traced to intrinsic variability in the fabrication process and is a serious problem affecting the process yield. And yet, a lack of unified simulation framework and statistically relevant physical models means that it has not been possible to quantify the exact impact of process variability at the module level.

Another important concern is a lack of physical understanding of reliability issues [3] that affect the intrinsic lifetime of TFPV. Obviously, the extrinsic reliability concerns (e.g. humidity, corrosion, inverter failure) must be addressed; but once these are solved, the intrinsic reliability concerns will ultimately control the lifetime of TFPV technologies. A particularly complex intrinsic reliability issue common to all thin-film technologies is the problem of partial shadowing in modules [4]. This problem requires an integrated device circuit analysis, because the exact impact of partial shadowing depends not only on device characteristics, but also module and array configurations.

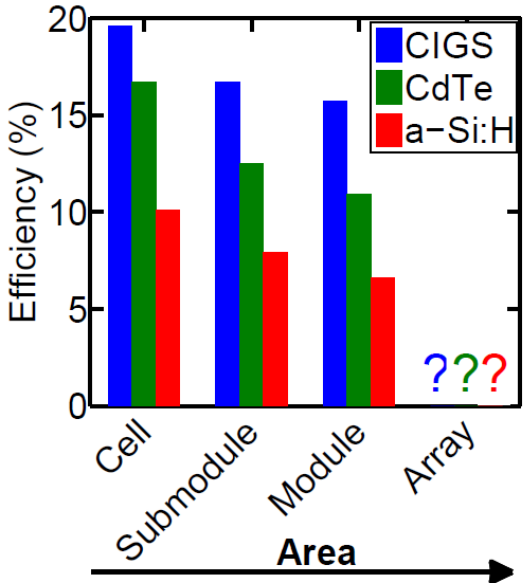

Fig. 1. Bars compare the efficiencies of different thin film PV technologies, showing the significant redcution in efficiency for large areas. Also highlighted, is the lack of clarity at system level efficiency in the field

In this paper, we develop such a combined device and circuit modeling framework and systematically analyze the following two problems. First is the efficiency loss from device to module level due to process variability, and next is the problem of partial shadowing under operating conditions, for an illustrative example of a-Si:H p-i-n technology. We use a physics based equivalent circuit for the cell, embedded in a 2D SPICE simulation framework, which is capable of incorporating statistical parameter fluctuations. Our variability analysis illustrates how module efficiency and yield are influenced by shunt variability and contact sheet resistance (R_S). Moreover, we use the system level analysis to show the limitations of bypass diodes in avoiding shadow induced reverse stress, and explore its long term reliability implications.

978-1-4577-1680-5/12/$26.00 ©2012 IEEE

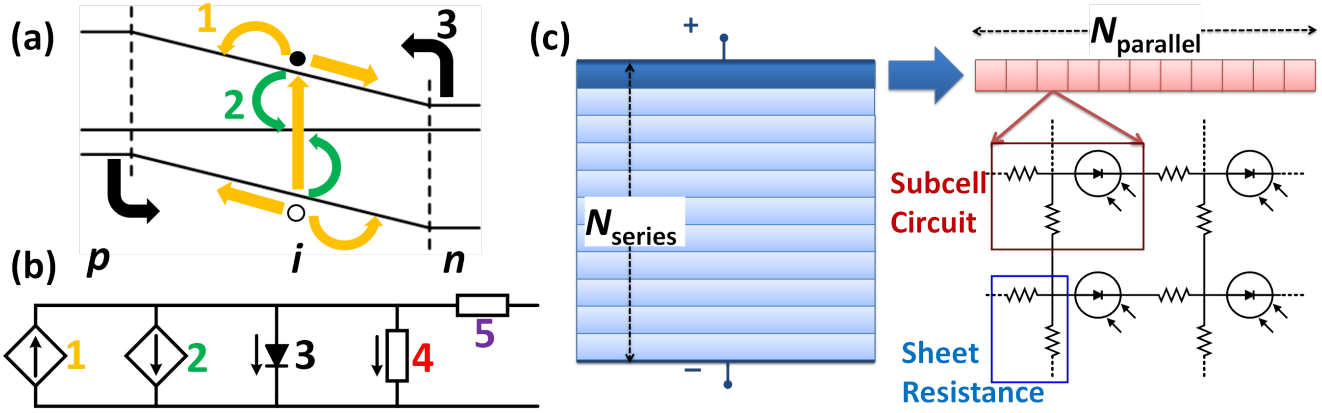

Fig. 2. (a) Schematic showing the band diagram of a p-i-n solar cell with voltage dependent collection (marked 1), bulk recombination (marked 2) and dark injection (marked 3) current components. (b) Equivalent circuit of the p-i-n cell incorporating all the photo and dark current components as shown in (a), as well as the parasitic shunt current (marked 4) and series resistance of transparent conductors (marked 5). (c) Schematic of typical thin film module with N_{series} cells in series. For simulations each cell is subdivided into $N_{parallel}$ subcells (red) connected in series-parallel using contact sheet resistance R_S. Each subcell is represented by the equivalent circuit shown in (b), with shunt current values varying from one cell to next.

II. Simulation Framework

We begin by creating generalized, physics based equivalent circuit for the thin film solar cell. In order to do this we must accurately account for voltage dependencies of all the generation and recombination processes, as well as statistical distribution of shunts. Fig. 2a shows the band diagram of a p-i-n solar cell under short circuit condition. The generation and recombination fluxes (1 and 2 in Fig. 2a) are marked explicitly in order to demarcate and analyze their contributions. In case of a-Si:H p-i-n solar cell, all these fluxes can be modeled analytically under reasonable assumptions, namely;

(a) the thickness of i-layer is much larger than the p/n layers;
(b) electric field inside the i-layer is constant and is given by $\mathcal{E} = (V - V_{bi})/d$, where V_{bi} is the built in potential and is the thickness of i-layer;
(c) the generation rate G_0 is constant across i-layer [5].

Under these assumptions, we can solve the drift-diffusion equations exactly for no recombination case, and calculate the voltage dependent photocurrent (marked 1) and Shockley injection current with ideality factor 1 (marked 3) [6]. We then use first order perturbation approximation to calculate the bulk recombination using the electron/hole profiles obtained from the previous solution. This gives us the generation dependent bulk recombination component (marked 2), and the dark bulk recombination current with ideality factor 2 (incorporated in flux 3) [7]. The expressions for these various current components are given below as;

$$J_{photo} = qG_0 d\left[\coth\left(\frac{q(V-V_{bi})}{2k_BT}\right) - \frac{2k_BT}{q(V-V_{bi})}\right], \quad (1)$$

$$J_{rec,ph} \approx \frac{G_0 d^3}{2\mu_{eff}\tau_{eff}(V-V_{bi})}, \quad (2)$$

$$J_{rec,dark} \approx \frac{2k_BT}{V-V_{bi}}\frac{n_i}{\tau}d\exp\left(\frac{qV}{2k_BT}\right). \quad (3)$$

Here, k_B is Boltzmann constant, T is absolute temperature, and μ_{eff} and τ_{eff} are effective carrier mobilities and lifetimes, respectively. Corresponding to each flux, a circuit component can be added to the equivalent circuit for voltage dependent collection (1) [6], bulk recombination (2) [7], and dark current (3) as shown in Fig. 2b. Note that for a-Si:H cells where carrier lifetimes are small and i-layer is thick, dark current ideality factor is close to 2, and the use of equation (3) is justified. Finally, the random parasitic shunt current (I_{SH}) is represented as a voltage dependent resistor (marked 4 in Fig. 2a). This non-Ohmic conductance is used to account for space-charge-limited (SCL) current characterized by power law voltage dependence given by;

$$I_{SH} = \frac{9\epsilon\mu_c(\gamma)A_{SH}}{8}\frac{V^{\gamma+1}}{L_{SH}^{2\gamma+1}}. \quad (4)$$

Here, ϵ is the material permittivity, and A_{SH} and L_{SH} denote the shunt area and thickness, respectively. And, the power exponents and effective mobility μ_c are determined by the trap distribution inside the bandgap (characterized by the parameter γ) [8]. These intrinsic shunts are typically formed due to local metal incursion in absorber layers through thin emitter layers, and show similar SCL behavior for different thin film PV technologies [9]. Since, these shunts are parasitic in nature, their magnitude varies from one location to other, which results in performance loss and variability at module level. In this equivalent circuit approach, we incorporate this variability of I_{SH} to analyze the module level performance. Further details of the complete model, as well as its experimental verifications for different types of TFPV technologies, will be discussed elsewhere.

A schematic of typical thin module is shown in Fig. 2c, showing thin wide strips of individual cells connected in series

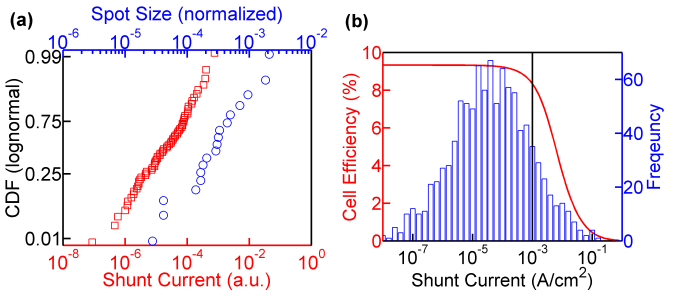

Fig. 3. (a) The lognormal distribution of I_{SH} magnitudes (red squares), is identical to the distribution of spot sizes (blue circles) obtained from independent dark thermography image in [9], providing independent verification for the observed distribution. (b) Cell efficiencies as a function of I_{SH} (red line), in relation to the lognormal I_{SH} (blue bars) for a reasonably good process. It shows that only a small fraction of cells (where $I_{SH} > \sim$1mA marked) deviate significantly from maximum cell efficiency (9.6% here).

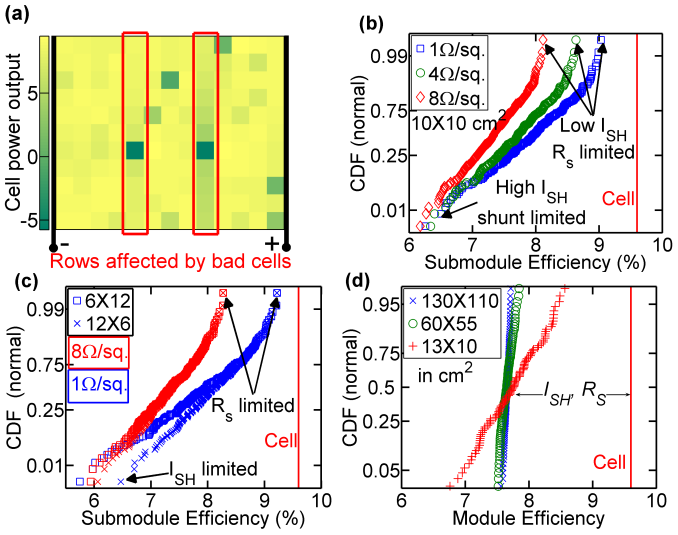

Fig. 4. (a) 2D plot of individual cell power outputs in a submodule showing the worst cells (black) *consuming* the output of neighboring cells in the row (highlighted). The extent of this effect on neighbors is R_S determined. (b) Submodule (10x10 cm^2) efficiency distributions (symbols) for different R_S but identical I_{SH} distributions show that high η tail is R_S limited, and low η tail is I_{SH} limited. (c) Distinction between series (crosses) and parallel (squares) connection schemes for submodules, for low (1 Ω/sq., blue) and high (8 Ω/sq., red) R_S case, matters only for high I_{SH} and low R_S case. (d) Area effect on module efficiency distribution, for identical shunt distributions, showing reduction in variance with constant η, due to shunt limited efficiency in this case.

with laser scribing. For module simulations it is subdivided in 1x1 cm^2 subcells, each represented with the equivalent circuit shown in Fig. 2b, and connected in series-parallel configuration by contact sheet resistance (marked 5 in Fig. 2a, R_S) [10]. The resultant circuit is simulated using commercial HSPICE software for Monte-Carlo analysis of variability. This not only allows a physical simulation of module characteristics, but also allows one to connect the modules in various configurations and evaluate their implications, as discussed in following sections. A free version of the simulator, based on Berkeley SPICE3, is available at nanohub.org [11].

III. Shunt Induced Variability

A. Physics and statistics of shunt current

We find the process-induced shunt formation is an important source of time-zero variability of solar cells. It is therefore important to accurately account for the physics and statistics of shunt conduction in the module level simulations. In order to account for the SCL shunt physics, the equivalent circuit in Fig. 2b includes a non-Ohmic shunt current element with power law voltage dependence; i.e. $I_{SH} = I_{SH0}V^{\beta}$, where power exponent β is about 2-3 [8]. Moreover, it has been reported that the magnitude I_{SH0} at subcell level in TFPV follows a lognormal distribution, as shown in Fig. 3a [12]. This can be independently corroborated by the spot size distribution from reverse dark thermography images [13]. The spot sizes in these images correspond to the strength of local shunt current. Interestingly, the size distribution of these spots also shows a lognormal behavior (Fig. 3a). This is in good agreement with the lognormal distribution observed from independently measured shunt current values.

At subcell level (lab scale samples), efficiency (η_C) is a strong function of the shunt current magnitude I_{SH0}, as shown in Fig. 3b (line). Fortunately, for cells and modules fabricated with reasonable process control, η_C is adversely affected only for a small fraction of cells, as dictated by lognormal shunt distribution (bars, Fig. 3b). However, even a small fraction of heavily shunted regions can have a disproportionately large impact on module efficiency as discussed next.

B. Submodule simulation R_S vs. R_{SH}

At module level, many cells are connected in series, and the interaction between the less shunted cells (high η_C) and highly shunted cells (low η_C) must be considered carefully. Fig. 4a shows the power output of each individual subcell connected in a submodule with 10 cells in series each 10x1 cm^2 in size. Here, each square represents a 1x1 cm^2 subcell with different shunt current values. The dark subcells are the heavily shunted ones, and in fact they consume the power output of the neighboring cells, and affect the power output from the entire row/cell. The ability of the bad cells to affect its neighbors is determined by the sheet resistance of contact materials (TCO in this case). Therefore, the effect of shunt variability at module level must be understood in terms of interplay between I_{SH} and R_S.

The first consequence of this interplay is evident in Fig. 4b, which shows the effect of R_S on the efficiency distribution of a 10x10 cm^2 submodule. These distributions are obtained from Monte-Carlo simulations of submodules with spatially random shunts (taken from identical shunt distributions, Fig. 3). We assume that shunt is the only varying parameter from one subcell to next. Note that the high efficiency tail of distribution, associated with low shunt values, is limited by R_S and improves for lower R_S values, because resistive dissipation is lower. In contrast, the efficiency of the heavily shunted submodules is dictated by I_{SH}, independent of R_S. This is because in these submodules a lot of power is dissipated locally by large shunt currents, hence, the interaction of

neighboring cells plays little role in the overall module output.

C. Submodule simulation - Series vs. Parallel

This insight about shunt and sheet resistances also helps us compare the series (high voltage) vs. parallel (high current) connection schemes in presence of shunts. Fig. 4c shows that configuration does not matter for high R_S or low I_{SH}. This is because, for high R_S, as well as for low I_{SH}, the cross-coupling among neighboring cells is suppressed, and the gap between series and parallel is small. Only for high shunting case with low R_S, the series connection scheme shows better performance. This is because, the low R_S value allows the bad cells to affect even the farther neighboring cells. And therefore, the series configuration with smaller number of neighboring cells performs better.

D. Submodule to module level

Fig. 4d shows the efficiency CDF for varying module sizes from about $\sim$100 cm^2 (submodule size) to typical $\sim$1 m^2 (module size). Note that variance of efficiency distribution reduces with module size, but mean remains constant. This is because, in this case, the module efficiencies are limited by shunts and the extent of effect of bad cells is small. Therefore, as the module area becomes larger the effect of interactions between neighboring cells is reduced and the distribution becomes narrower. Note that these simulations reproduce the realistic gap between η_C and η_M of 2-4% (see Fig. 1), *without using any external fitting parameters*, underscoring the effectiveness of this approach.

This analysis also offers key insights into the problem of lower module efficiencies. First of all, it says that while η_C-η_M gap can be traced essentially to random I_{SH} and contact R_S, but the variability of η_M is not due to shunts (as their influence is localized by R_S). Therefore, any variability observed in production of thin film modules, must necessarily reflect macroscopic defects and manufacturing control. Another interesting observation from this result is that the mean of submodule efficiencies can provide a good estimate of the full size module efficiency, which can help speed up process evaluation and process qualification.

IV. Shadow Degradation

Next we demonstrate how this integrated modeling approach can be scaled to analyze system reliability issues as well. We focus on the problem of shadow degradation, caused by partial shadowing of series connected thin film modules [14]. This is a well known issue for all PV technologies, but poses a unique challenge in case of thin film PV. This is because, TFPV cells are shaped like thin wide stripes and their shapes must be considered to understand the impact of shading correctly. Moreover, while incorporation of bypass diodes inside TFPV modules is possible [15]; it is not straightforward, and hence not widely used. This means that a partial shade on such TFPV panels can result in severe reverse stress on shaded cells, *even when the modules themselves have an external bypass diode*, as discussed below.

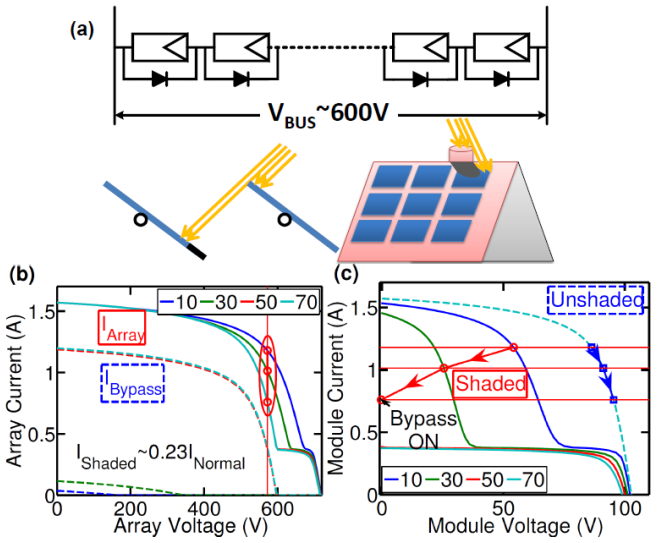

Fig. 5. (a) Schematic of typical TFPV string of modules attached to a 600V DC bus, which is the system considered here. (b) Schematics of possible partial shading caused by nearby modules or other objects, usually when sun is at shallow angles. (c) 1D simulation of partial shading for $V_{BUS} = 572V$, showing the array (solid) and bypass diode (dashed) currents for different number of shaded cells (out of a module of 110 series connected cells). (d) IV curves for shaded (solid) and unshaded (dashed) modules in a string, with operating points (circles shaded, squares unshaded), showing that bypass diode turns on only after significant partial shadowing, and large drop in output current.

We study the partial shading of a module in a series string of 7 typical sized a-Si:H modules with 110 cells in series, each 130x1 cm^2 in area. These modules are connected to system DC bus operating at 572V (Fig. 5a). This DC bus voltage is kept constant and all strings feed this supply bus. In the event of partial shading due to nearby objects, the shaded area is only illuminated by scattered (diffuse) sunlight, which is $\sim$20% of direct sunlight for typical visibility conditions [16]. Partial shadows of varying sizes and positions may be caused by a nearby object or neighboring module (see schematics in Fig. 5a); therefore, it is important to evaluate all possible shadow sizes to assess their impact.

A. Limitations of bypass diodes

We first perform a 1D simulation to understand the behavior of external bypass diodes. In this simulation, each 130x1 cm^2 is represented by the equivalent circuit, and the IV characteristics are obtained for varying number of shaded cells in the module. Fig. 5b shows the results of this circuit simulation for a string of 7 modules, each with external bypass diodes, for partial shade on one of the modules. We find that while each module has a bypass diode, it does not turn on until shading exceeds $\sim$50% of a panel, as seen from the array and bypass diode current values in Fig. 5b. Shading continues to reduce the array current (because the voltage is fixed) until the bypass diode of shaded module turns on and clamps the array current.

This can be understood by comparing the operating points of shaded and unshaded modules as a function of shading

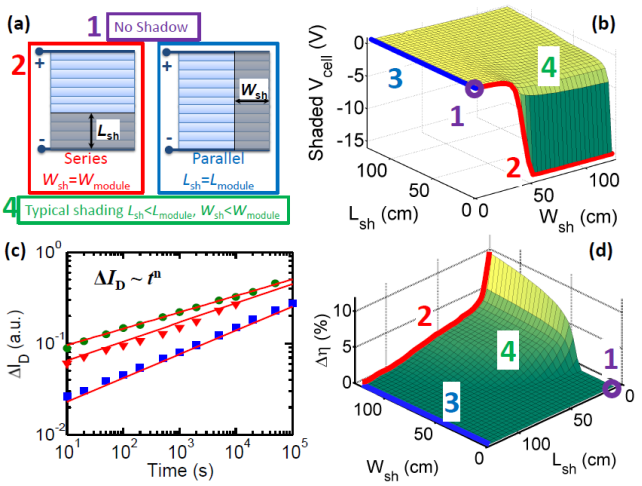

Fig. 6. (a) 2D shading configurations compared in this analysis, including no shade (marked 1), series shadow (marked 2), parallel shadow (marked 3) and intermediate shading (marked 4) shading conditions, defined in terms of shaded length L_{sh} and width W_{sh} as shown. (b) Voltage across shaded cells for different scenarios. The highest reverse stresses occur, when L_{sh} is small and $W_{sh} = W_{module}$ (marked 2 and highlighted red). On other hand, in case of parallel shading, where Wsh is small with $L_{sh} = L_{module}$ (marked 3 and highlighted blue), the shaded cells do not go into reverse bias. Intermediate shading (marked 4) may result in varying degrees of moderate reverse stress. (c) Moderate reverse stress (case marked 4) results in parametric time dependent increase in dark current ($\Delta I_D \propto t^n$), with power exponent $n \approx 0.2 - 0.25$, for a-Si:H cells [14]. (d) Due to this parametric shadow degradation, the expected efficiency loss over 25 year operation of module with 2 hours of partial shadow each day, for different shading scenarios.

conditions (see Fig. 5c). As the shading increases, the shaded module voltage reduces and the unshaded module voltage increases to keep the current continuous and the fixed array voltage. And, the bypass diodes kick in only when the total voltage across shaded module can no longer be positive. This means that the bypass diodes do not play any role until a very large area of the module is shaded. But, as we show next, the shaded cells can experience high reverse biases even for small shadows. And, since the output does not drop significantly for small shadows the bypass diodes remain off and cannot protect the shaded cells.

B. Shadow degradation

The 1D circuit simulation approach discussed above, is useful for analyzing the role of bypass diodes and understanding the array level behavior. To understand the effects at cell level, however, we must consider the various shading configurations including the different shadow lengths and widths. Fig. 6a shows the various cases of shadowing considered, with shadow length (L_{sh}) and width (W_{sh}) as shown. L_{sh} and W_{sh} are varied from 0 to module dimensions to account for all different shadow sizes. Fig. 6a highlights the cases with $W_{sh} = W_{module}$ (defined as *series* shading) and $L_{sh} = L_{module}$ (defined as *parallel* shading), in order to illustrate the importance of shadow orientation in case of edge shading.

Fig. 6b shows the surface plot of voltage across shaded cells, for all different shadow conditions. It clearly shows that reverse breakdown stresses are caused when the entire width is shaded (series shading, marked 2, red). On the other hand, if all cells are shaded partially along the module width (parallel shading, marked 3, blue), then the shaded cell voltage stays positive. In realistic situations, where the shadows will cover only a part of module length and width, the shaded cell voltage can vary between forward to moderate reverse biases (marked 4)

It has been reported earlier [14] that these moderate stresses in a-Si:H cells result in a parametric time dependent increase in dark current, as shown in Fig. 6c. By combining the information about shadow stress voltage (Fig. 6b), and the power law degradation in dark current (Fig. 6b), we can calculate the effect of partial shadow on performance of shaded cells, over the module lifetime. For a module lifetime of 25 years, with 2 hours of shadow per day, the degradation expected for various shading scenarios can be as high as 10% (Fig. 6d), which is comparable to light induced degradation in a-Si:H cells [17].

This integrated approach provides clear insights into the origins and impact of partial shading in thin film PV. The circuit analysis highlights the limitation of external bypass diodes in avoiding reverse stress across individual cells, and distinguishes the worst case scenarios from the more likely moderate shading cases. An important observation from this analysis is the impact of shadow orientation, which suggests that mounting the panels sideways to avoid series shading can prevent the worst case scenario for the panels. The physics of device degradation then tells us what amount of shadow related performance loss can be expected for a panel experiencing regular partial shade.

V. Conclusion

We have presented an end to end modeling approach that scales from device to system level, and is capable of incorporating statistics and physics alike. We demonstrated the utility of this approach by analyzing the shunt variability and shadow induced reliability problem in TFPV. For analyzing the gap between cell and module efficiencies, we incorporated the statistics of shunt conduction in full 2D model simulation. Our analysis demonstrates that interplay of I_{SH} and R_S can explain the lower efficiency of large area modules (compared to cell efficiency), but the variability at module level itself arises from macroscopic defects. We also analyzed the problem of partial shadowing of modules, and studied device implications, in context of array configuration. We have illustrated the utility of our model by using a-Si:H technology; however, the model is flexible enough to be adapted to any TFPV technology (e.g., CIGS or CdTe), for gaining quantitative insight into their associated variability and reliability issues.

Acknowledgment

This work was supported by SRC-ERI Network for Photovolotaic Technology grant 204900. M. A. A. was partially supported by US DOE funded EFRC award number DE-SC0001085. We acknowledge the computational resources

from Network for Computational Nanotechnology, Purdue University. We would also like to thank Biswajit Ray from Purdue University, and Dr. Michel Frei, Applied Materials for useful discussions and feedback.

REFERENCES

[1] M. A. Green, "Thin-film solar cells: review of materials, technologies and commercial status," *Journal of Materials Science: Materials in Electronics*, vol. 18, no. S1, pp. 15–19, Apr. 2007.

[2] M. A. Green, K. Emery, Y. Hishikawa, W. Warta, and E. D. Dunlop, "Solar cell efficiency tables (Version 38)," *Progress in Photovoltaics: Research and Applications*, vol. 19, no. 5, pp. 565–572, Aug. 2011.

[3] C. R. Osterwald and T. J. McMahon, "History of accelerated and qualification testing of terrestrial photovoltaic modules: A literature review," *Progress in Photovoltaics: Research and Applications*, vol. 17, no. 1, pp. 11–33, Jan. 2009.

[4] M. A. Alam, S. Dongaonkar, Y. Karthik, S. Mahapatra, D. Wang, and M. Frei, "Intrinisic reliability of amorphous silicon thin film solar cells," in *2010 IEEE International Reliability Physics Symposium*. IEEE, 2010, pp. 312–317.

[5] R. S. Crandall, "Modeling of thin film solar cells: Uniform field approximation," *Journal of Applied Physics*, vol. 54, no. 12, p. 7176, 1983.

[6] R. Sokel and R. Hughes, "Numerical analysis of transient photoconductivity in insulators," *Journal of Applied Physics*, vol. 53, no. 11, p. 7414, 1982.

[7] J. Merten, J. Asensi, C. Voz, A. Shah, R. Platz, and J. Andreu, "Improved equivalent circuit and analytical model for amorphous silicon solar cells and modules," *IEEE Transactions on Electron Devices*, vol. 45, no. 2, pp. 423–429, 1998.

[8] S. Dongaonkar, K. Y, D. Wang, M. Frei, S. Mahapatra, and M. A. Alam, "On the Nature of Shunt Leakage in Amorphous Silicon p-i-n Solar Cells," *IEEE Electron Device Letters*, vol. 31, no. 11, pp. 1266–1268, Nov. 2010.

[9] S. Dongaonkar, J. D. Servaites, G. M. Ford, S. Loser, J. Moore, R. M. Gelfand, H. Mohseni, H. W. Hillhouse, R. Agrawal, M. A. Ratner, T. J. Marks, M. S. Lundstrom, and M. A. Alam, "Universality of non-Ohmic shunt leakage in thin-film solar cells," *Journal of Applied Physics*, vol. 108, no. 12, p. 124509, 2010.

[10] G. T. Koishiyev and J. R. Sites, "Impact of sheet resistance on 2-D modeling of thin-film solar cells," *Solar Energy Materials and Solar Cells*, vol. 93, no. 3, pp. 350–354, 2009.

[11] E. E. Gurrola, S. Dongaonkar, and M. A. Alam, "PVpanel Sim." [Online]. Available: https://nanohub.org/tools/pvpanelsim

[12] S. Dongaonkar, K. Y., S. Mahapatra, and M. A. Alam, "Physics and Statistics of Non-Ohmic Shunt Conduction and Metastability in Amorphous Silicon pin Solar Cells," *IEEE Journal of Photovoltaics*, vol. 1, no. 2, pp. 111–117, Oct. 2011.

[13] V. Sittinger, F. Ruske, W. Werner, B. Szyszka, B. Rech, J. Hüpkes, G. Schöpe, and H. Stiebig, "ZnO:Al films deposited by in-line reactive AC magnetron sputtering for a-Si:H thin film solar cells," *Thin Solid Films*, vol. 496, no. 1, pp. 16–25, 2006.

[14] S. Dongaonkar, Y. Karthik, D. Wang, M. Frei, S. Mahapatra, and M. A. Alam, "Identification, Characterization and Implications of Shadow Degradation in Thin Film Solar Cells," in *Reliability Physics Symposium (IRPS), 2011 IEEE International*. Monterey, CA: IEEE, 2011, pp. 5E.4.1 – 5E.4.5.

[15] J. Armstrong, S. Wiedeman, and L. Woods, "US Patent 6,690,041," Feb. 2004. [Online]. Available: http://www.google.com/patents/US6690041

[16] "The Intensity of Solar Radiation." [Online]. Available: http://www.homer.com.au/webdoc/science/solar/SolarRadiationIntensity.html

[17] W. Tzeng, H. Tsai, and S. Lee, "Degradation and annealing characteristics of amorphous silicon-hydrogen alloys after a long-time test," *Journal of Applied Physics*, vol. 62, no. 5, pp. 1856–1860, 2009.